Sustainable Energy & Fuels

ROYAL SOCIETY OF CHEMISTRY

PAPER

View Article Online
View Journal | View Issue

Cite this: *Sustainable Energy Fuels*, 2021, **5**, 1488

Anisotropic mass transport using ionic liquid crystalline electrolytes to suppress lithium dendrite growth†

Deepesh Gopalakrishnan,[a] Samia Alkatie,[a] Andrew Cannon,[b] Sathish Rajendran,[a] Naresh Kumar Thangavel,[a] Neha Bhagirath,[a] Emily M. Ryan*[b] and Leela Mohana Reddy Arava *[a]

Received 16th October 2020
Accepted 29th January 2021

DOI: 10.1039/d0se01547d

rsc.li/sustainable-energy

Lithium metal as an anode has been widely accepted due to its higher negative electrochemical potential and theoretical capacity. Nevertheless, the existing safety and cyclability issues limit lithium metal anodes from practical use in high-energy density batteries. Repeated Li deposition and dissolution processes upon cycling lead to the formation of dendrites at the interface which results in reduced Li availability for electrochemical reactions, disruption in Li transport through the interface and increased safety concerns due to short circuiting. Here, we demonstrate a novel strategy using Ionic Liquid Crystals (ILCs) as the electrolyte cum pseudo-separator to suppress dendrite growth with their anisotropic properties controlling Li-ion mass transport. A thermotropic ILC with two-dimensional Li-ion conducting pathways was synthesized and characterized. Microscopic and spectroscopic analyses elucidate that the ILC formed with a smectic A phase, which can be utilized for wide temperature window operation. The results of electrochemical studies corroborate the efficacy of ILC electrolytes in mitigating dendrite formation even after 850 hours and it is further substantiated by numerical simulation and the mechanism involved in dendritic suppression was deduced.

Introduction

Research on rechargeable Li metal-based batteries has been amplified as Li metal can deliver a specific capacity of ~3862 mA h g^{-1}, which positions it as a promising component in portable energy devices, electric vehicle systems, robotics, and other grid storage technologies.[1–4] However, meeting the demand for portable energy storage devices with high energy density remains a challenge. In this scenario, Li–O_2 and Li–S batteries are capable of delivering ultra-high energy densities and are considered as next generation energy storage systems.[5] Unfortunately, the intrinsic issues instigated by electrode/electrolyte interactions causing problems in terms of safety and cyclability in these batteries hinder their practical implementation in certain applications.[6,7] In particular, heterogeneous anode materials can lead to the formation of dendrites on their surface, which has a longstanding negative affect on the Li battery (LiB) performance in terms of safety and cycle life.[8,9] The effects of dendrite growth on the stability of battery cycling can be due to the increased interfacial resistance and poor coulombic efficiencies which lead to cell short-circuiting, cell failure, and explosion.[8,10] Hence, prevention of dendrite formation is necessary to employ Li metal as an anode in batteries.

At the Li metal/electrolyte interface, Li-ions react with electrons during the charging process and electrochemically get reduced and deposited onto the Li metal anode.[11,12] Impurities and protrusions on the anode surface cause the nucleation of dendritic Li structures with faster kinetics and inconsistent deposition.[13] Li mass transport is the main factor for dendrite growth, which depends on many physical processes such as advection, ion migration and reactions at the electrode/electrolyte interface.[14,15] Large variations in the Li^+ ion concentration gradient across the surface of the anode also appear to encourage the deposition and Li dendrite formation. Researchers have made tremendous efforts to suppress dendrite growth through various techniques such as electrode modification, controlling the Li morphology, designing different cell configurations by introducing protective layers and conducting scaffolds, implementing different kinds of electrolytes including solid-state, gel electrolytes, and more.[9,10,16] The limited success of these strategies call for a better approach towards dendrite suppression.

Recent theoretical studies based on liquid crystals suggest that the anisotropic properties of the electrolyte can control Li-ion mass transport and pave the way for the suppression of

[a]*Department of Mechanical Engineering, Wayne State University, Detroit, MI 48202, USA. E-mail: larava@wayne.edu*

[b]*Department of Mechanical Engineering, Boston University, Boston, MA 02215, USA. E-mail: ryanem@bu.edu*

† Electronic supplementary information (ESI) available. See DOI: 10.1039/d0se01547d

dendrite growth.[12] Also, modelling and simulation studies indicate that the electrolyte which enables high ionic conductivity and lithium transference numbers (t_{Li^+}) near unity at the reaction sites can reduce the concentration gradient and thereby the dendrite growth.[17,18] Among the several electrolytes explored, ionic liquid crystals (ILCs) are promising due to their exceptionally efficient 1D, 2D and 3D anisotropic ion-conduction pathways and capability to form robust solid electrolyte interfaces (SEI) with reduced resistance because of their liquid-like mobility.[19–24] Recently, rod like ILCs consisting of a cyclic carbonate derivative moiety and lithium bis(trifluoromethylsulfonyl)imide (LiTFSI) have been studied in Li-ion batteries.[25] However, to date, there have been no reports on how the anisotropic properties of ILCs could influence dendrite growth on Li anodes.

Here, we developed a novel imidazolium based thermotropic ILC material from a long-alkylated phenol, 3-pentadecyl phenol (3-PDP). The characterization of the ILC revealed a bent core structure with self-assembled molecules exhibiting high ionic conductivity at both RT and elevated temperatures. We report that these ILCs with their anisotropic properties can act as a pseudo separator-cum-electrolyte and control the Li ion concentration gradient at the electrolyte–anode interface, which helps in controlling Li ion mass transport and thereby suppressing dendrite growth, as shown in Scheme 1. To complement the experimental results, numerical simulations were performed to explore the mechanism of dendrite suppression based on the properties of the ILC electrolyte.

Experimental section

Characterization of ILC electrolytes

The ionic conductivity and anisotropic nature of ILC electrolytes were determined by using electrochemical impedance spectroscopy (EIS) and differential scanning calorimetry (DSC) analysis. ^{1}H NMR spectroscopy was carried out to confirm the formation of the target ILC. Further, wide angle X-ray diffraction (WAXD), small angle X-ray scattering (SAXS) and polarizing optical microscopy (PLOM) studies were used to determine the crystal data and orientation of the additive containing LC.

Anisotropy conductivity measurements

Anisotropic ionic conductivity was measured in both directions parallel and perpendicular to the self-assembled layers using the alternating current impedance technique. Anisotropy in the ionic conductivity of LCs was analyzed with a pair of comb shaped gold electrodes (cell A) and a pair of indium tin oxide (ITO) plates (cell B). First, gold was sputtered onto a glass plate in a comb shape by leaving a 1 mm distance between the teeth and a sidewise width of approximately 0.3 mm. The thickness of the sputtered gold was about 0.8 μm. Both the cells were filled with the compound mixtures and their orientation was confirmed using a polarizing microscope. Ionic conductivity parallel to the oriented layer was measured using cell A, and the one perpendicular to the oriented layer was obtained by using cell B. In cell B, a pair of ITO electrodes were separated with a thickness of 30 μm using a Teflon spacer. In both cases, homeotropic alignment of the sample mixtures was observed.

Interfacial mesoscale modeling

Numerical simulations use a multiphase reactive transport model based on smoothed particle hydrodynamics (SPH) which is a Lagrangian particle-based method. SPH was first developed for astrophysical problems and it has been adapted to solve fluid dynamics, multiphase flows, and reactive transport by discretizing the continuity equations.[12,26–28] The model used for the studies presented in this work is based on previous modeling of dendrite growth.[12,29,30] The details of the model equations and implementation can be found in the work by Tan *et al.*[12] This model was developed using open-source software called Large-scale Atomic/Molecular Massively Parallel Simulator (LAMMPS).[31]

Electrochemical measurements

The electrodeposition of Li in LC based electrolytes was performed using galvanostatic cycling of Li|LiTFSI–ILC|Li symmetric lithium cells in which the lithium striping process was carried out at a constant current which resembles a conventional lithium metal battery. The symmetric cells were fabricated using CR2032 cells with Li electrodes of 10 mm in size on both sides of the separator made of Teflon with a hole of 1.6 mm diameter at the center facilitating ionic mobility between the Li electrodes and preventing any other side reactions. The prepared novel ILC electrolyte with an optimized amount of LiTFSI was poured in the hole of the separator. Symmetric cell cycling from −1 to 1 V was conducted on an

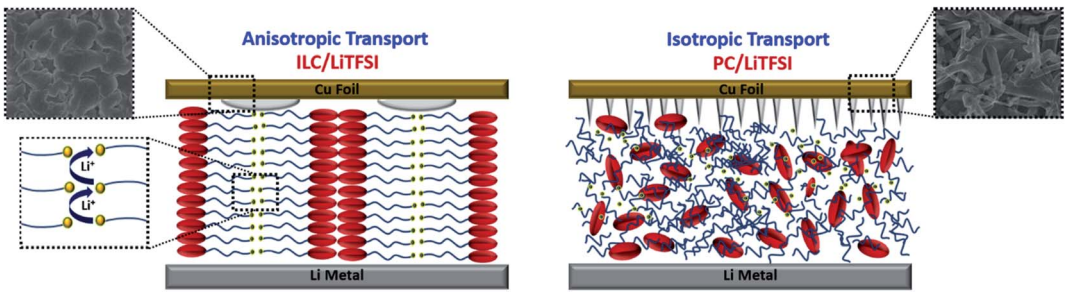

Scheme 1 Schematic representation of the proposed mechanism of anisotropic Li mass transport effect towards dendrite suppression when compared to the isotropic transport.

Arbin electrochemical workstation with a current density of 0.1 mA cm^{-2} at 60 °C. The charging and discharge times were restricted to 3 hours. The control experiment with the electrolyte containing LiTFSI and PC was also carried out for comparison studies. EIS studies were conducted in the frequency range 1 Hz to 1 MHz using a Bio-Logic electrochemical workstation. Li|Au cells for electrochemical stability measurements were fabricated by using Au (blocking electrode) as the working electrode and Li as the reference and counter. Gold sputtered stainless steel was used as the blocking electrode for this experiment.

Results and discussion

Details pertaining to the synthesis of ILC, 3-(12-(3-pentadecylphenoxy)dodecyl)-1-methylimidazole_3-3ium hexafluoro-phosphate (PDDMHP) are explained and provided in the ESI.† The formation of the target compound is schematically represented in Scheme S1† and it is confirmed by proton nuclear magnetic resonance (^{1}H NMR) analysis. In the NMR spectrum (Fig. S1†) of PDDMHP, the triplet at a δ value of 0.9 ppm corresponds to the terminal methyl protons of the pentadecyl chain. Peaks in between 1 and 3 ppm are ascribed to the methylenic protons present in the pentadecyl side chain and dodecyl spacer chain. Methylenic protons present adjacent to the electronegative O^- and N^- atoms give characteristic triplets at 3.9 and 4.2 ppm, respectively. A sharp singlet at 3.8 ppm is due to the protons of the methyl groups attached directly to the imidazolium ring. Aromatic protons in the phenyl ring give characteristic peaks in between 6.8 and 7.2 ppm, whereas the protons in the imidazole ring produce peaks at 7.8 and 9.2 ppm. Thus, ^{1}H NMR analysis clearly confirmed the formation of an imidazolium based ionic liquid crystal.

Further, Fourier transform infrared spectroscopy (FT-IR) analysis was carried out to confirm the functional group present in the as synthesized compound and the corresponding spectra are shown in Fig. S2.† The presence of an alkyl chain having symmetric and asymmetric C–H stretching vibrations can be observed as multiple peaks in the range of 2800–3000 cm^{-1}. The peaks from 3000 to 3200 cm^{-1} correspond to the C–H vibration modes of aromatic rings. C–C stretching, and C–N bending vibrations can be observed from the peaks in the range of 1600–1585 cm^{-1}. The peak at 1455 cm^{-1} is attributed to the C–H alkyl deformation, whereas a peak at 1189 cm^{-1} indicates the C–N stretching vibration. C–O–C stretching of alkyl aryl ether is visible with the presence of a peak at 1158 cm^{-1}. Finally, P–F stretching vibrations of the PF^6 anion is observed at 820 cm^{-1}. To validate the fact that the synthesized imidazolium based ILCs exhibited a thermotropic mesophase, we performed differential scanning calorimetry (DSC) thermograms measurements. To analyze the thermotropic phase transition of the synthesized compound, the sample was heated and cooled from 200 to −20 °C. On a heating ramp, PDDMHP displays a transition from the crystalline to liquid crystalline phase, *i.e.* smectic A (SmA) at a temperature of 55 °C and an isotropic phase at 165 °C (Fig. 1a). On cooling from the isotropic melt, PDDMHP transforms into the smectic A phase again at 165 °C and returns to its crystalline nature at 25 °C. These features can be observed clearly in the DSC spectrum shown in Fig. 1a. The phase transition temperatures and enthalpy changes of PDDMHP are derived from DSC traces and are listed in Table S1.†

Though the precise phase cannot be identified using DSC, the level of enthalpy change involved at the phase transition gives an estimate of the type of phase involved.[32,33] The structural changes, which occur during temperature variation, reflect the enthalpy changes. The enthalpy changes of the liquid crystallite to an isotropic liquid transition indicate that the LC phase is smectic A (SmA).[34] Furthermore, the type of mesophase that the compound exhibits is confirmed by using optical polarizing microscopy in conjunction with DSC analysis. The image (Fig. 1b) was taken while cooling from the isotropic phase starting at 165 °C. During cooling, the randomly aligned or disordered ionic liquid crystal molecules are aligned together to form supramolecular organized liquid crystalline phases by several noncovalent interactions such as electrostatic, ionic assembling and van der Waal's interactions, helping to form a mesophase in the compound with different extents of order. The images show that the liquid crystals are in the smectic A phase at temperatures ranging from 55 to 165 °C and are shown in Fig. 1b. Wide angle X-ray diffraction (WAXD) was carried out at different temperatures to examine the phase transformation of the synthesized compound and is shown in Fig. 1c. At room temperature, PDDMHP was highly crystalline due to the strong ionic interactions between the charged counterparts and long alkyl chains. PDDMHP was heated to form amorphous phases without any characteristic peaks, showing a complete transformation to the isotropic phase above 170 °C. On cooling from the melt, the quasi-crystalline nature reappeared with a few of the reflections at a temperature below 100 °C, confirming the recrystallization of the melt to an anisotropic liquid crystalline phase. The high intensity peaks at the LC and crystalline phases are attributed to the stacking of imidazolium cations. The emergence of moderately crystalline peaks when the isotropic melt is cooled below 100 °C could be corroborated to the formation of the anisotropic LC phase. This observation is in well agreement with the DSC analysis.

Thermotropic liquid crystalline phase formation of the compound is observed with small-angle X-ray scattering (SAXS) analysis (Fig. 1d). At room temperature, the SAXS pattern of PDMHP displays two peaks with *d*-spacing values of 39 Å and 19.6 Å owing to the crystalline order of the ionic liquid crystal. Increasing the temperature to 50 °C, the liquid crystalline phase begins to emerge, and in addition to the peaks mentioned before, a shoulder initiates at a lower scattering vector. SAXS analysis of the compound at 140 °C clearly illustrates the formation of a liquid crystalline phase as the crystalline peaks completely disappear and a sharp self-assembly peak with a *d*-spacing of 43.9 Å persists. This sharp peak corresponds to the self-assembly of PDDMHP by means of non-covalent interactions such as alkyl chain interdigitation, van der Waal's interactions and ion–lone pair interactions. The expected layered 2D conduction pathways allow ion transportation in both parallel and perpendicular directions. This is confirmed by carrying out

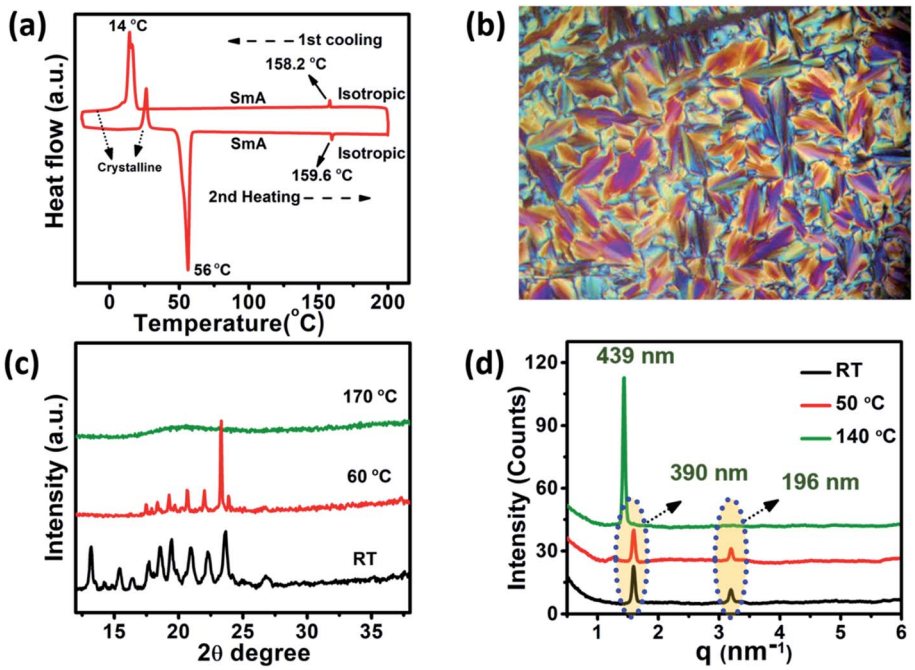

Fig. 1 (a) DSC heating and cooling scans of PDDMHP showing thermotropic behavior. (b) PLOM images showing the SmA phase of the PDDMHP. (c) WAXD patterns of PDDMHP at different temperature. (d) SAXS pattern of PDDMHP.

anisotropic ILC measurements in both directions for ILCs at varying temperature. The ionic conductivity value of each cell (gold electrode and ITO based electrode) is different at each temperature (SmA phase), explaining the anisotropic nature of these ILCs (Fig. 2a and b). Both gold and ITO electrode cell configurations are shown in Fig. 2c. The ionic conductivity (IC) between the gold teeth (parallel to the smectic layer) is found to be higher when compared to that between ITO plates perpendicular to the layer. The IC values at various temperatures in both directions are summarized in Fig. 2d.

Electrochemical studies

To further use LCs as an electrolyte for LiBs, the synthesized compounds were mixed with an optimized amount of LiTFSI. This was to form 2D ion conducting pathways through ion–dipole interactions between the imidazole group and Li ions in the salt.[25,35] It is expected that the concentration of salt has an impact on liquid-crystalline behavior, along with its viscosity and ionic conductivity. To verify, lithium composites of different ratios of 9 : 1, 3 : 1 and 1 : 1 were prepared by solvent evaporation of a corresponding solution in tetrahydrofuran. The ionic conductivities of these electrolytes were measured repeatedly in an ambient atmosphere by AC impedance spectroscopy over a frequency range of 1 Hz to 1 MHz at 60 °C with amplitude 10 mV to ensure reproducibility. Fig. 3a shows the resultant electrochemical impedance Nyquist plot and the corresponding equivalent circuit and the magnified portion is shown in Fig. 3b. The solution resistance from the fitted impedance spectra is measured and the ionic conductivity is mathematically calculated and plotted against temperature (1000/T) (Fig. 4a).[36,37]

The expression for ionic conductivity calculations is $\sigma = (1/R_s)(l/a)$ where l is the thickness of the samples and a is the area of the electrode. The measured ionic conductivities in the order of 10^{-4} S cm^{-1} are obtained in the SmA phase and are shown in Table 1. There is an increase in ionic conductivity as the temperature is increased and when the material transforms into the liquid crystalline phase, SmA phase which can be due to the oriented conductive pathways creation. The higher conductivities at elevated temperatures at SmA phases (<60 °C) are due to the lower viscosity and broader 2D conducting pathways.[38] These 2D arrangements of the ion conducting groups can provide opportunities for lithium ions to travel in both X and Y-directions, overcoming the defects confronted throughout the pathways while continuing directional movement. Among the different compositions of ILC and Li salt, 9 : 1 ratio shows high ionic conductivity. The optimized amount of LiTFSI was found to be 9 equimolar (the molar ratio of PDMHP to LiTFSI was 9 : 1) and this mixture was selected as the electrolyte for further electrochemical measurements.

Ion conductivity measurements are carried out by lithium transference number (t_{Li^+}) studies to find the suitability of these electrolytes for better Li-ion battery performance. The Li transference number (t_{Li^+}) is calculated at RT and 60 °C *via* EIS before and after the chronoamperometric technique (CA) test. In Fig. 4b, the chronoamperometry and EIS results of both the cells with and without the ILC are shown. At room temperature (Fig. S3 and S4†), t_{Li^+} is found to be 0.062 whereas at elevated temperature (100 °C), it increases to 0.32. It is well known that the coulombic interaction between the cation and anion dominantly plays a major role in the transference and mobility of Li^+ ions. Although conventional liquid electrolytes

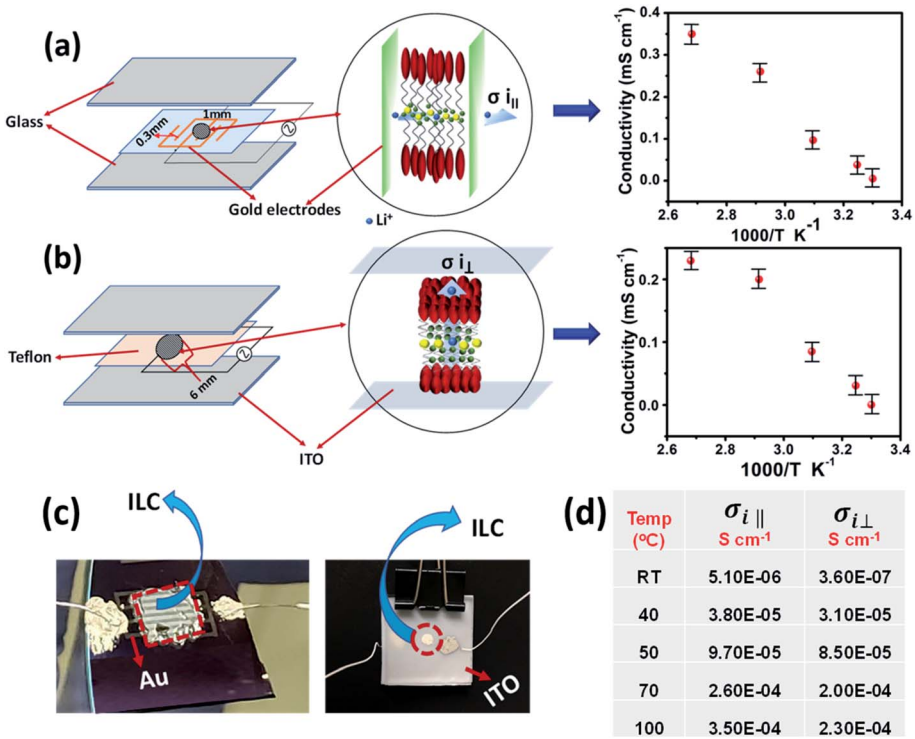

Temp (°C)	$\sigma_{i\parallel}$ S cm^{-1}	$\sigma_{i\perp}$ S cm^{-1}
RT	5.10E-06	3.60E-07
40	3.80E-05	3.10E-05
50	9.70E-05	8.50E-05
70	2.60E-04	2.00E-04
100	3.50E-04	2.30E-04

Fig. 2 Anisotropic ionic conductivity measurements. (a) Structure of the comb shaped gold electrode cell for horizontal ionic conductivity analysis of PDDMHP, (b) structure of the ITO electrode cell for perpendicular ion conductivity analysis, the (c) gold electrode cell and ITO electrode cell, and (d) table with parallel and perpendicular ionic conductivity in PDDMHP at different temperatures varying from RT, 40, 50, 70 to 100 °C.

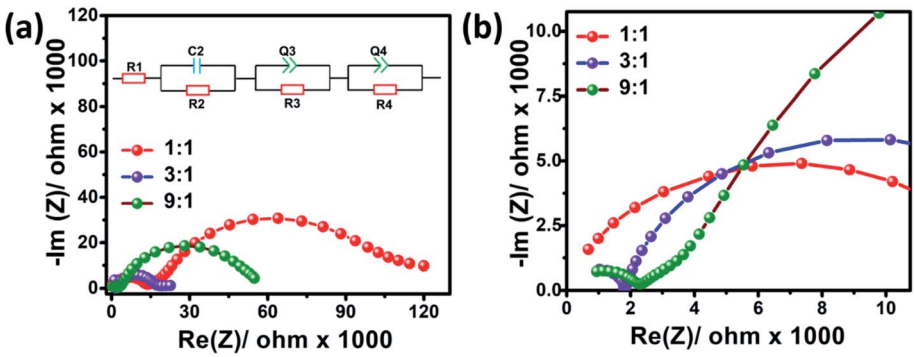

Fig. 3 (a) Nyquist plot of different compositions of PDDMHP with LiTFSI and the corresponding equivalent circuit, and (b) magnified plot.

exhibit high ionic conductivity, the transference number used to be low. This is certainly due to the strong preferential solvation of Li^+ by the anion and the strong coulombic interaction between them, resulting in a bulky solvation shell around Li^+ compared to that of typical anions.[39] However, in our case, as the cation is bigger, the coulombic interaction between the larger cation and anion will become weaker which tends to increase the mobility of cations over anions.[40] As per previous reports, it is expected that with a higher t_{Li^+} value, the concentration gradient will be reduced by removing anion depletion induced electric fields near the electrode/electrolyte interface, which limits the nucleation of Li dendrites.[41] According to Monroe and Newman's simulation studies, when t_{Li^+} approaches unity, the ion concentration gradient near the Li anode is suppressed by extending the sands time *i.e.* stopping or delaying the dendrite growth.[41,42] The synergistic effect of higher ionic conductivity and appropriate t_{Li^+} values for parallel Li-ion conduction thus controls the concentration gradient near the electrode surface through effectively regulating Li ion mass transfer, which eventually inhibits the dendrite formation and its growth. This is further evidenced by both the experimental and the interfacial computational simulations as given below.

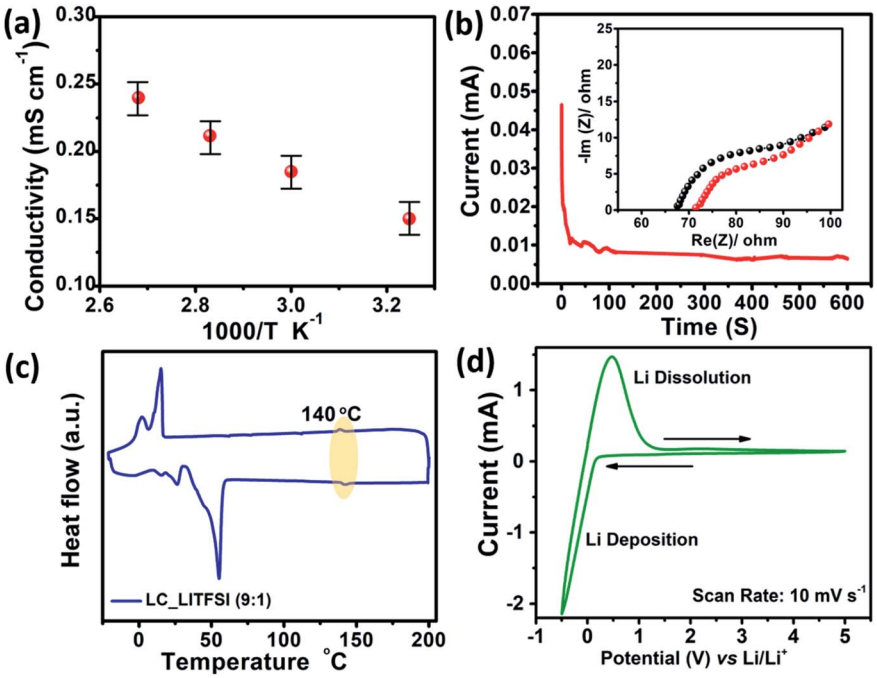

Fig. 4 (a) Ionic conductivity of optimized LiTFSI/PDDMHP, (b) Li transference number measurements: chronoamperometry profile for PDDMHP as the electrolyte in a symmetric Li/(LiTFSI/PDDMHP)/Li cell with an applied voltage of 10 mV, the Nyquist plot for the symmetric Li/(LiTFSI/PDDMHP)/Li cell before and after polarization, (c) DSC measurements of optimized LiTFSI/PDDMHP, and (d) electrochemical stability of the formulated ILC based electrolyte.

Table 1 Ionic conductivities of different lithium composites containing PDDMPH and LiTFSI at different ratios of 9 : 1, 3 : 1 and 1 : 1, respectively

Composition	σ (S cm^{-2})
ILC/LiTFSI, 1 : 1	1.37×10^{-4}
ILC/LiTFSI, 3 : 1	1.72×10^{-4}
ILC/LiTFSI, 9 : 1	1.85×10^{-4}

To corroborate the ILC properties after the addition of LiTFSI salts, we performed DSC measurements on the ILC–LiTFSI (9 : 1) mixture, as shown in Fig. 4c. These thermotropic ILCs have a wide liquid crystalline window that provides the potential of utilizing their anisotropic nature over a wide range of temperatures. DSC measurements confirmed that the mixture was still in the LC phase, with small changes in its anisotropy or mesophase window (Fig. 4c). With the incorporation of Li salt (LiTFSI) into this ILC, there was a slight decrease in the anisotropic window, although it still extended up to 140 °C. The smectic A phase transitions underwent small changes with the incorporation of LiTFSI. This is attributed to the fact that the in-plane packing of mesogens within the smectic layer is disturbed by the addition of bulky LiTFSI salts. Also, the ILC electrolyte is expected to show higher ionic conductivity and is chosen as an electrolyte for electrochemical measurements. The isotropization temperature decreases for the mixture containing the ILC and LiTFSI in a 9 : 1 molar ratio, although the SmA phase is still present over a wide temperature range. The SmA phase with higher molecular motion exhibited higher molecular conductivity as expected at an elevated liquid crystalline temperature, making it preferable for use as an electrolyte in LiBs. As previously mentioned, the ionic conductivity is satisfactorily enhanced to 1.85×10^{-4} at a temperature of 60 °C due to the lower viscosity and highly efficient oriented ion conducting pathways of the SmA phase. Thus, the ILC : LITFSI mixture in a 9 : 1 molar ratio can act as an electrolyte with its persisting anisotropic nature enabling controlled Li ion mass transport.

The electrochemical stability of the ILC–LiTFSI composite based electrolyte was evaluated using cyclic voltammetry using a Li|Au blocking electrode cell at an elevated temperature of 60 °C where the SmA – anisotropic phase was observed (Fig. 4d). The measurements were conducted in a potential range from 0 to 5 V *versus* Li/Li$^+$ at a scan rate of 10 mV s^{-1} and the voltammogram is shown in Fig. 4d. There is an increase and decrease in the current near 0 V *versus* Li/Li$^+$ during the anodic and cathodic sweep which is due to the Li deposition and dissolution on the gold sputtered stainless steel substrate. The absence of any peak over the Li deposition and dissolution region indicates that there is no significant electrolyte decomposition at a higher voltage, which suggests stable Li transportation, and electrochemical reactions at the electrodes in the presence of an ILC electrolyte in a wide potential window. Thus, the electrolyte mixture with an optimized molar ratio of the ILC and LiTFSI shows a higher electrochemical stability without any decomposition in a higher voltage range, indicating the efficient transport of Li ions between the electrodes without undergoing any electrochemical reactions. This can be

attributed to the presence of mesogens acting as an ion conducting moiety.

Electrochemical cycling performance

After formulating the electrolyte, dendrite suppression studies were carried out where the anisotropic nature of the ILC is believed to regulate the ion concentration gradient at the interface. The electrodeposition of Li in the ILC based electrolytes was investigated using galvanostatic cycling of Li|ILC–LiTFSI|Li symmetric lithium cells in which the lithium striping process is carried out at a constant current of 0.032 mA. The symmetric cells contain Li counter/reference and working electrodes on both sides of a hollow Teflon spacer filled with the ILC electrolyte. Symmetrical Li/Li cells with and without the ILC as the electrolyte were tested at a current density of 0.1 mA cm^{-2} and a temperature of 60 °C to evaluate the long-term electrochemical cycling stability of the Li electrodes. Li/ILC–LiTFSI/Li showed a stable Li plating/stripping behavior in the presence of an anisotropic electrolyte with a gradual increase in polarization, which can be clearly seen in the voltage hysteresis. The difference between Li stripping and plating voltages represents the voltage hysteresis and is principally determined from the applied current density, electrode/electrolyte interfacial properties and charge transfer resistance. A symmetrical Li/Li cell containing LiTFSI/propylene carbonate (PC) as an electrolyte shows a stable voltage hysteresis without any irregular oscillations when compared with the cell having ILCs; however, dendrite induced internal short circuit is seen after 400 hours as shown in Fig. 5a. In contrast, the cell with the ILC electrolyte is able to cycle stably for more than 850 hours as the anisotropic electrolyte medium can improve the Li^+ mass transport between the major dendrite growth sites, and thereby form dendrites in a uniform and compact manner. The Li metal after cycling was removed from the cycled cells and was analyzed using FE-SEM, as shown in Fig. 5b and c. The cycled Li from the PC/LiTFSI cell showed a very rough surface with uneven chunks of Li metal, which can be attributed to the repeated uneven Li plating/stripping from the surface. On the other hand, the cycled Li from the ILC/LiTFSI cell was relatively much smoother with very small corrugations. The relatively smoother Li indicates stable cycling of the cell with minimal loss of Li during the formation of the SEI, which is due to the relatively lower surface area. This is also one of the reasons for the lower polarization of the cell.

The morphology of the Li deposited was analyzed using Cu/Li cells, where Cu was the working electrode and Li was the reference and the counter. Li deposition onto Cu foil was carried out at a current density of 0.25 mA cm^{-2} for 4 hours, after which the coin cells were disassembled to obtain the Cu foil for analysis using FE-SEM. Fig. 6 and S5† show the morphology of the Li deposition using PC/LiTFSI and ILC/LiTFSI electrolytes. In agreement with the previous reports,[43,44] Li plating using PC/LiTFSI resulted in sharp needle like deposits, as seen in Fig. 6a, b and S5a.† The diameter of the needle like structure was found to be in the range between 400 nm and 0.2 μm, which can easily penetrate through any separator easily that can lead to the short circuiting of the cell. Such formation of dendritic Li structures is reported in several other popular electrolytes affecting the cyclability of Li metal batteries.[45,46] In contrast, the ILC/LiTFSI deposits showed no such needle like morphology that correspond to the formation of Li dendrites. The morphology was spherical in shape with a diameter of 0.5 to 1.2 μm, as shown in Fig. 6c and d. It is difficult for such a bigger sized morphology with curved edges to penetrate any separator. Also, the surface area is also

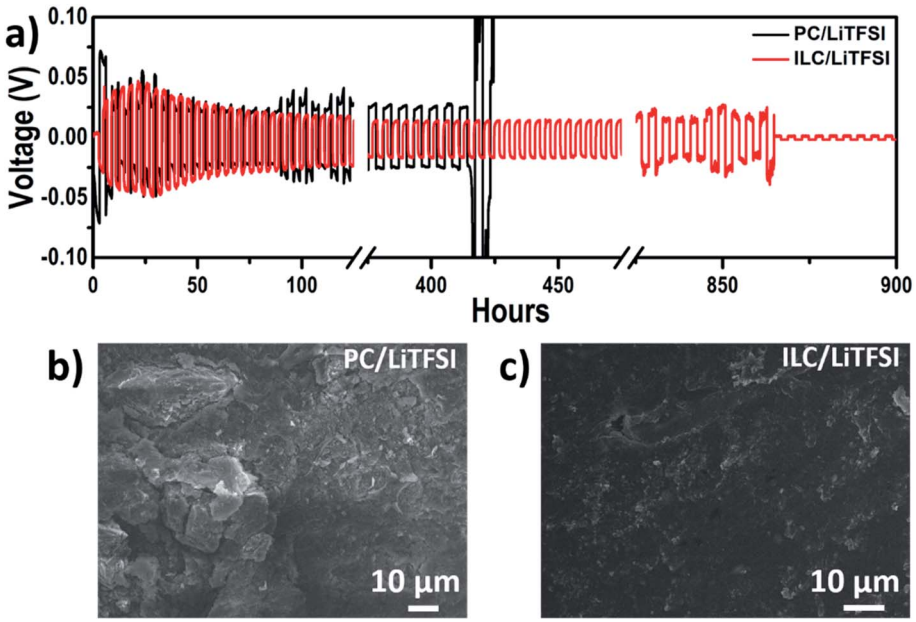

Fig. 5 (a) Electrochemical Li plating/stripping of symmetric Li|ILC/LITFSI|Li and Li|PC/LiTFSI|Li cells with a current density of 0.1 mA cm^{-2}; postmortem analysis (FE-SEM) of the cycled Li electrode of (b) PC/LiTFSI and (c) ILC/LiTFSI cells.

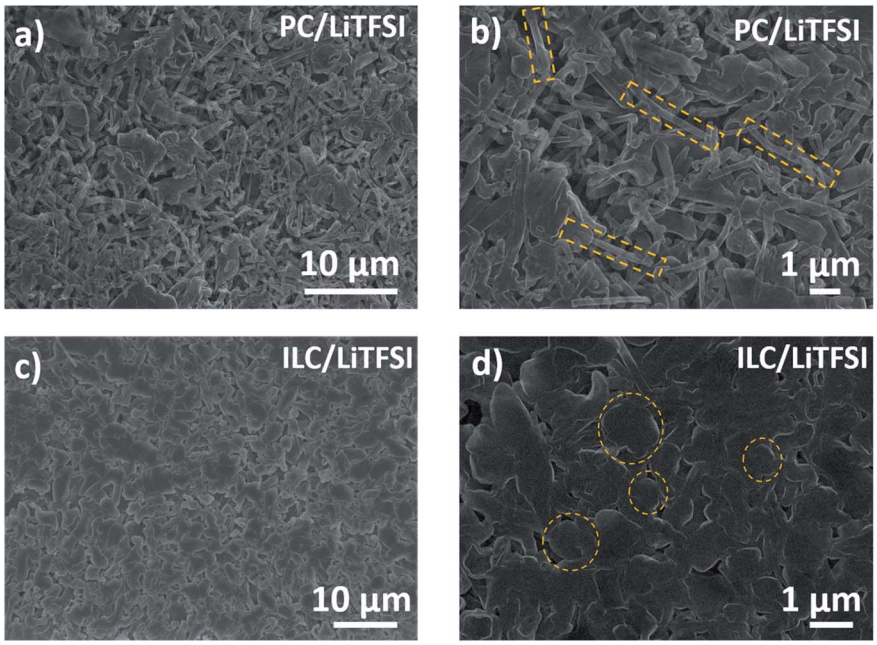

Fig. 6 FE-SEM Li deposition morphological studies of (a and b) PC/LiTFSI, and (c and d) ILC/LiTFSI.

drastically reduced as it is a well-known fact that a sphere possesses the lowest surface area compared to any other morphology, which increases the efficiency of the Li deposition process by reducing the amount of Li that is consumed in the formation of the SEI. Further, the Li deposited using ILC/LiTFSI was found to be uniform and compact (Fig. S5b and c†), which can be ascribed to the horizontal growth in the *y*-direction due to the anisotropic type of mass transport occurring in the electrolyte.

Simulation of the interfacial reactive transport

To understand the local transport mechanisms that lead to dendrite suppression in the ILC electrolyte, a numerical model is developed to study the reactive transport near the electrode–electrolyte interface. A Lagrangian particle-based modeling method known as smoothed particle hydrodynamics (SPH) is used to investigate how changes in local ion transport properties affect the growth of dendrites. To approximate the ILC electrolyte, a pseudo-separator like structure is simulated. Based on the experimental characterization of the ILC electrolyte, it is assumed that ILC supra molecules in the electrolyte have a semi-ordered structure that can be approximated as a separator of rod-like particles. The rod-like particles in the order of a few microns in length are dispersed throughout the electrolyte in different orientations. The effects of particle orientation are varied from completely parallel to the anode surface, to randomly oriented (Fig. 7a). Simulations are used to elucidate how the ILCs affect local transport and dendrite growth. Dendrite growth increases as the supramolecules align perpendicular to the anode surface while a random orientation or alignment favoring the direction parallel to the anode reduces the dendrite growth, as seen in Fig. 7a. This can also be seen in the contour plots of local mass flux in Fig. 7b and the growth rate of Fig. 7c.

The anisotropic mass transport effect is proposed as a novel concept towards dendrite growth suppression in Li batteries and the corresponding scheme is shown in Fig. 7d. The concentration gradient near the anode–electrolyte interface can be controlled by inducing these directional properties in Li ion batteries with the help of anisotropic ILCs.[47] From the numerical models of Fig. 7b, the ILC supramolecules restrict local mass transport near the electrode interface. This leads to slower dendrite growth. The parallelly aligned liquid crystalline molecules with their layered structure control the Li ion mass transfer, which in turn affects the Li ion concentration in the vicinity of the electrode. The Li ion concentration gradient near the electrode/electrode interface is the major reason for dendrite growth after nucleation. This smaller ion concentration gradient is reflected in the uniform SEI formation, which controls the dendrite growth rate.

The effects of local transport mechanisms on dendrite growth are also seen in the numerical models of the interface as seen in Fig. 7b. The concentration gradients drive Li transport near the interface. Along the surface of the anode (bottom of Fig. 7a and b), the gradient goes toward zero in the cases of parallel, random, and misaligned parallel structures. This is due to the high tortuosity through these structures. In the case of the perpendicular structure the tortuosity is roughly one and the separator has little effect on the local mass flux. The lower mass flux along the anode leads to the suppression of dendrite growth and a longer battery lifetime. The low mass flux indicates an even distribution of Li concentration across the anode surface, which leads to a more even Li deposition. This allows for slower and more uniform growth, resulting in less harmful dendrites. In the presence of an anisotropic electrolyte medium,

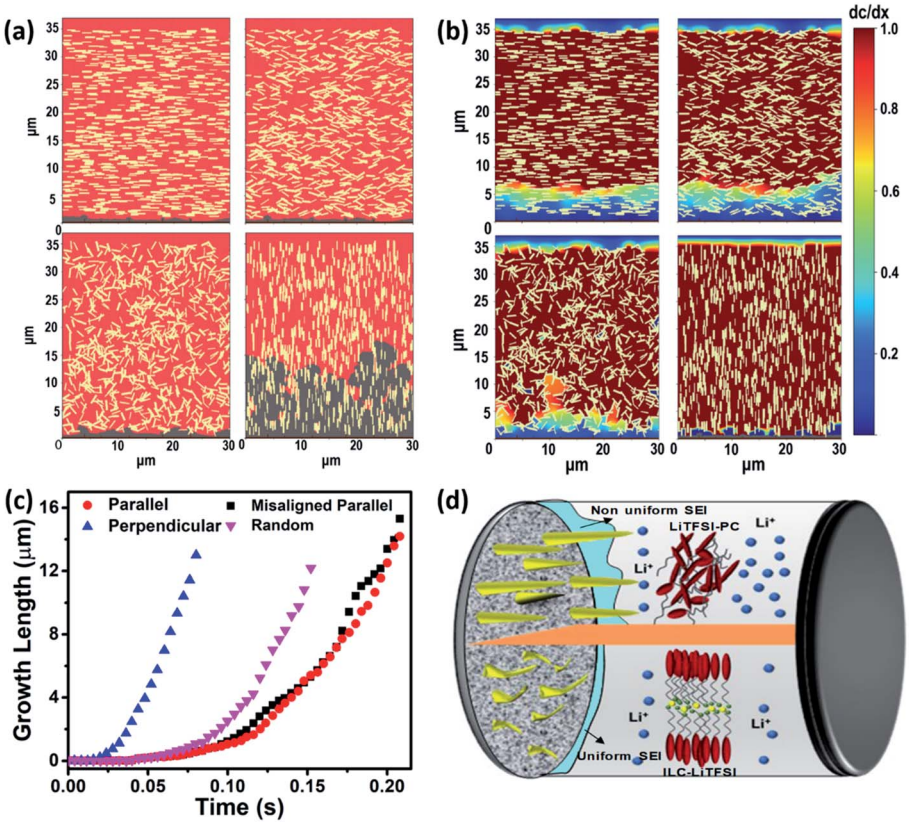

Fig. 7 (a) Simulations domains for structures parallel, misaligned parallel, random, and perpendicular to the anode. (b) Local mass flux through the separators as dendrites grow into the separator from the anode (at $y = 0$). (c) Growth rate of dendrites over time for each separator structure. (d) Graphical representation of the proposed mechanism.

major dendrites form at the interspace between the initial dendritic nucleation sites, while the already formed dendrites are suppressed. This is supported by the numerical models as seen in the parallel and random cases of Fig. 5b. In the anisotropic case, Li ion diffusion to the major dendrite growth region decreases and hinders the replenishment of Li^+ ions in that region, prompting Li^+ ions to deposit in the adjacent dendrite free regions and thus leading to the formation of more compact and flat dendrites. Thus, these thermotropic ILC electrolytes with their ability to orient themselves in different directions to control Li mass transport and thereby suppress dendrite growth can act as pseudo separator.

Conclusions

In summary, we have shown the synthesis of anisotropic liquid crystalline electrolytes and their efficacy in the mitigation of dendrite growth by reducing the Li ion concentration near the dendrite tip. The numerical models have demonstrated the mechanism of ILC electrolytes for dendrite suppression and better Li diffusion control. This anisotropic mass transport effect can suppress dendrite growth without sacrificing the battery performance. New thermotropic ILCs with a SmA phase, for wide temperature window operation, containing 2D ion conducting pathways have been prepared and well characterized using various microscopic and spectroscopic techniques. The anisotropic ion conductivity was probed by conducting EIS measurements using both gold electrodes and ITO electrodes in both parallel and perpendicular directions consecutively. ILC : LiTFSI in the 9 : 1 molar ratio was tested for dendrite studies and it showed that highly ionic conducting pathways and near unity t_{Li^+} can greatly reduce the Li ion concentration at the anode surface and retard dendrite formation and growth. This is further exemplified through continuous lithium plating/stripping around 850 h with negligible change in polarization on extended cycling, suggesting the compactness and robustness of the anisotropic ILC electrolyte mitigating dendrite formation. The demonstrated results reveal that anisotropic ILCs are promising LIB electrolytes for a long cell cycle life while ensuring safety by controlling dendritic parasitic reactions in the cells.

Conflicts of interest

The authors declare no competing financial interest.

Acknowledgements

This material is based upon work supported by the National Science Foundation under grant no. 1751472.

References

1 J. M. Tarascon and M. Armand, *Nature*, 2001, **414**, 359.
2 P. G. Bruce, S. A. Freunberger, L. J. Hardwick and J.-M. Tarascon, *Nat. Mater.*, 2011, **11**, 19.
3 F. Croce, G. B. Appetecchi, L. Persi and B. Scrosati, *Nature*, 1998, **394**, 456.
4 J. C. Jones, S. Rajendran, A. Pilli, V. R. Lee, N. Chugh, L. M. R. Arava and J. A. Kelber, *J. Vac. Sci. Technol., A*, 2020, **38**, 023201.
5 P. G. Bruce, L. J. Hardwick and K. M. Abraham, *MRS Bull.*, 2011, **36**, 506–512.
6 N. Nitta, F. Wu, J. T. Lee and G. Yushin, *Mater. Today*, 2015, **18**, 252–264.
7 J. B. Goodenough and K.-S. Park, *J. Am. Chem. Soc.*, 2013, **135**, 1167–1176.
8 X.-B. Cheng, R. Zhang, C.-Z. Zhao and Q. Zhang, *Chem. Rev.*, 2017, **117**, 10403–10473.
9 Y. Guo, H. Li and T. Zhai, *Adv. Mater.*, 2017, **29**, 1700007.
10 D. Wang, W. Zhang, W. Zheng, X. Cui, T. Rojo and Q. Zhang, *Adv. Sci.*, 2016, **4**, 1600168.
11 K. Nishikawa, T. Mori, T. Nishida, Y. Fukunaka and M. Rosso, *J. Electroanal. Chem.*, 2011, **661**, 84–89.
12 J. Tan, A. M. Tartakovsky, K. Ferris and E. M. Ryan, *J. Electrochem. Soc.*, 2016, **163**, A318–A327.
13 O. Crowther and A. C. West, *J. Electrochem. Soc.*, 2008, **155**, A806–A811.
14 J.-G. Zhang, W. Xu and W. A. Henderson, in *Lithium Metal Anodes and Rechargeable Lithium Metal Batteries*, Springer International Publishing, Cham, 2017, pp. 5–43, DOI: 10.1007/978-3-319-44054-5_2.
15 C. T. Love, O. A. Baturina and K. E. Swider-Lyons, *ECS Electrochem. Lett.*, 2015, **4**, A24–A27.
16 S. Rajendran, N. K. Thangavel, K. Mahankali and L. M. R. Arava, *ACS Appl. Energy Mater.*, 2020, **3**(7), 6775–6784.
17 P. Barai, K. Higa and V. Srinivasan, *J. Electrochem. Soc.*, 2017, **164**, A180.
18 K. Deng, J. Qin, S. Wang, S. Ren, D. Han, M. Xiao and Y. Meng, *Small*, 2018, **14**, 1801420.
19 M. Yoshio, T. Mukai, K. Kanie and M. Yoshizawa, *Adv. Mater.*, 2002, **14**, 351.
20 M. Yoshio, T. Kato, T. Mukai, M. Yoshizawa and H. Ohno, *Mol. Cryst. Liq. Cryst.*, 2004, **413**, 99–108.
21 Y. Uchida, T. Matsumoto, T. Akita and N. Nishiyama, *J. Mater. Chem. C*, 2015, **3**, 6144–6147.
22 M. Galiński, A. Lewandowski and I. Stępniak, *Electrochim. Acta*, 2006, **51**, 5567–5580.
23 R. Sasi, S. Sarojam and S. J. Devaki, *ACS Sustainable Chem. Eng.*, 2016, **4**, 3535–3543.
24 R. Sasi, K. B. Jinesh and S. J. Devaki, *ChemistrySelect*, 2017, **2**, 315–319.
25 J. Sakuda, E. Hosono, M. Yoshio, T. Ichikawa, T. Matsumoto, H. Ohno, H. Zhou and T. Kato, *Adv. Funct. Mater.*, 2015, **25**, 1206–1212.
26 E. M. Ryan, A. M. Tartakovsky and C. Amon, *J. Contam. Hydrol.*, 2011, **120–121**, 56–78.
27 J. J. Monaghan, *Rep. Prog. Phys.*, 2005, **68**, 1703.
28 E. M. Ryan and A. M. Tartakovsky, *J. Contam. Hydrol.*, 2011, **126**, 61–71.
29 J. Tan and E. M. Ryan, *J. Power Sources*, 2016, **323**, 67–77.
30 J. Tan and E. M. Ryan, *Int. J. Energy Res.*, 2016, **40**, 1800–1810.
31 S. Plimpton, *J. Comput. Phys.*, 1995, **117**, 1–19.
32 S. Singh and D. Dunmur, *Liquid Crystals: Fundamentals*, World Scientific Publishing Co Pte Ltd, Singapore, 2002.
33 S. Singh, *Phys. Rep.*, 2000, **324**, 107–269.
34 M. Subrao, D. M. Potukuchi, G. Sharada Ramachandra and P. Bhagavath, *Beilstein J. Org. Chem.*, 2015, **11**, 233–241.
35 A. Guerfi, M. Dontigny, P. Charest, M. Petitclerc, M. Lagacé, A. Vijh and K. Zaghib, *J. Power Sources*, 2010, **195**, 845–852.
36 Y. Lu, Z. Tu and L. A. Archer, *Nat. Mater.*, 2014, **13**, 961.
37 W.-K. Shin, A. G. Kannan and D.-W. Kim, *ACS Appl. Mater. Interfaces*, 2015, **7**, 23700–23707.
38 N. Schweikert, A. Hofmann, M. Schulz, M. Scheuermann, S. T. Boles, T. Hanemann, H. Hahn and S. Indris, *J. Power Sources*, 2013, **228**, 237–243.
39 K. M. Diederichsen, E. J. McShane and B. D. McCloskey, *ACS Energy Lett.*, 2017, **2**, 2563–2575.
40 T. Frömling, M. Kunze, M. Schönhoff, J. Sundermeyer and B. Roling, *J. Phys. Chem. B*, 2008, **112**, 12985–12990.
41 J. Jorne, *Nano Lett.*, 2006, **6**, 2973–2976.
42 L. Li, S. Li and Y. Lu, *Chem. Commun.*, 2018, **54**, 6648–6661.
43 R. Miao, J. Yang, Z. Xu, J. Wang, Y. Nuli and L. Sun, *Sci. Rep.*, 2016, **6**, 21771.
44 J. Qian, W. A. Henderson, W. Xu, P. Bhattacharya, M. Engelhard, O. Borodin and J. G. Zhang, *Nat. Commun.*, 2015, **6**, 6362.
45 F. Ding, W. Xu, X. Chen, J. Zhang, M. H. Engelhard, Y. Zhang, B. R. Johnson, J. V. Crum, T. A. Blake and X. Liu, *J. Electrochem. Soc.*, 2013, **160**, A1894.
46 F. Ding, W. Xu, G. L. Graff, J. Zhang, M. L. Sushko, X. Chen, Y. Shao, M. H. Engelhard, Z. Nie, J. Xiao, X. Liu, P. V. Sushko, J. Liu and J. G. Zhang, *J. Am. Chem. Soc.*, 2013, **135**, 4450–4456.
47 K. Goossens, K. Lava, C. W. Bielawski and K. Binnemans, *Chem. Rev.*, 2016, **116**, 4643–4807.